

Nature

September 2021, Volume 597 Issue 7876 Pages 370-375

<https://doi.org/10.1038/s41586-021-03805-8><https://archimer.ifremer.fr/doc/00723/83476/>**Archimer**<https://archimer.ifremer.fr>

Widespread phytoplankton blooms triggered by 2019–2020 Australian wildfires

Tang Weiyi ¹, Llorc Joan ^{2,3}, Weis Jakob ^{2,4}, Perron Morgane M. G. ², Basart Sara ³, Li Zuchuan ^{1,5}, Sathyendranath Shubha ⁶, Jackson Thomas ⁶, Sanz Rodriguez Estrella ⁷, Proemse Bernadette C. ², Bowie Andrew R. ^{2,8}, Schallenberg Christina ^{2,8}, Strutton Peter G. ^{2,4}, Matear Richard ^{9,*}, Cassar Nicolas ^{1,10,*}

¹ Division of Earth and Climate Sciences, Nicholas School of the Environment, Duke University, Durham, NC, USA

² Institute for Marine and Antarctic Studies, University of Tasmania, Hobart, Tasmania, Australia

³ Barcelona Supercomputing Centre, Barcelona, Spain

⁴ Australian Research Council Centre of Excellence for Climate Extremes, University of Tasmania, Hobart, Tasmania, Australia

⁵ Applied Ocean Physics and Engineering, Woods Hole Oceanographic Institution, Woods Hole, MA, USA

⁶ Plymouth Marine Laboratory, Plymouth, UK

⁷ Australian Centre for Research on Separation Science (ACROSS), School of Natural Sciences, University of Tasmania, Hobart, Tasmania, Australia

⁸ Australian Antarctic Program Partnership, University of Tasmania, Hobart, Tasmania, Australia

⁹ CSIRO Oceans and Atmosphere, Hobart, Tasmania, Australia

¹⁰ CNRS, Univ Brest, IRD, Ifremer, LEMAR, Plouzané, France

* Corresponding authors : Richard Matear, email address : richard.matear@csiro.au ; Nicolas Cassar, email address : nicolas.cassar@duke.edu

Abstract :

Droughts and climate-change-driven warming are leading to more frequent and intense wildfires^{1,2,3}, arguably contributing to the severe 2019–2020 Australian wildfires⁴. The environmental and ecological impacts of the fires include loss of habitats and the emission of substantial amounts of atmospheric aerosols^{5,6,7}. Aerosol emissions from wildfires can lead to the atmospheric transport of macronutrients and bio-essential trace metals such as nitrogen and iron, respectively^{8,9,10}. It has been suggested that the oceanic deposition of wildfire aerosols can relieve nutrient limitations and, consequently, enhance marine productivity^{11,12}, but direct observations are lacking. Here we use satellite and autonomous biogeochemical Argo float data to evaluate the effect of 2019–2020 Australian wildfire aerosol deposition on phytoplankton productivity. We find anomalously widespread phytoplankton blooms from December 2019 to March 2020 in the Southern Ocean downwind of Australia. Aerosol samples originating from the Australian wildfires contained a high iron content and atmospheric trajectories show that these aerosols were likely to be transported to the bloom regions, suggesting that the blooms resulted from the fertilization of the iron-limited waters of the Southern Ocean. Climate models project more frequent and severe wildfires in many regions^{1,2,3}. A greater appreciation of the links between wildfires, pyrogenic

aerosols¹³, nutrient cycling and marine photosynthesis could improve our understanding of the contemporary and glacial–interglacial cycling of atmospheric CO₂ and the global climate system.

Human activity is altering the global water and carbon cycles¹⁴. While the risk of drought associated with climate change varies regionally, warming and drying will increase the risk of more frequent and intense wildfires¹⁻³. In turn, wildfires are increasingly viewed as a first-order control on climate. Among other things, wildfires change the Earth's radiative forcing by emitting greenhouse gases and aerosols¹⁵. The feedbacks between climate and wildfires are complex and often poorly represented in climate models, leading to high uncertainty in future projections.

The austral summer of 2019-2020 was one of the most severe wildfire seasons in Australian history. Millions of hectares of vegetation were burned, having ecological, environmental and socio-economic impacts^{5,16}. It is estimated that nearly 3 billion animals may have died or been displaced¹⁷. According to a study by van der Velde published in this issue of *Nature*¹⁸, approximately 715 million tons of CO₂ (195 Tg C) were released into the atmosphere during the fire period, exceeding Australia's 2018 anthropogenic CO₂ emissions of 537.4 million tons (147 Tg C)¹⁹.

The 2019-2020 Australian wildfires (known in Australia as 'bushfires') also released an enormous amount of aerosols into the atmosphere^{6,7}. Aerosols can significantly influence terrestrial and marine biogeochemistry²⁰, via supplying soluble forms of nitrogen⁸, phosphorus⁹, and bio-essential trace metals including iron (Fe)^{10,13}. The High-Nutrient Low-Chlorophyll (HNLC) waters of the Southern Ocean are mostly iron-limited²¹. Delivery of Fe to these waters is believed to be an essential driver of oceanic primary production, atmospheric CO₂ uptake by the oceans, and to modify climate over geological timescales^{22,23}. In the open waters of the Southern Ocean, the dominant Fe sources are deep winter mixing²⁴, dust^{25,26}, hydrothermalism²⁷, and ice melt²⁸.

Here we provide a first assessment of how the 2019-2020 Australian wildfires stimulated an expansive phytoplankton response in the Southern Ocean. While the impact of wildfires on local terrestrial nutrient dynamics through soil erosion and aerosol deposition is well studied²⁹, our work demonstrates the potential of wildfires to impact marine ecosystems thousands of kilometers away through long-range atmospheric aerosol transport. During the 2019-2020 Australian wildfires, vast aerosol plumes from biomass burning were emitted into the atmosphere from southern and eastern Australia, as revealed by MODIS satellite aerosol retrievals (Extended Data Fig. 1a). Some aerosols and gases reached altitudes of up to 16 km, causing previously undocumented changes in stratospheric winds⁶ and further highlighting the intensity and uniqueness of the 2019-2020 Australian wildfires. Since aerosol optical depth (AOD) in the visible spectral range (at 550 nm) reflects bulk aerosol load in the atmospheric column, including desert dust, sea salt, sulfate, organic matter and black carbon, we use black carbon AOD estimated by the Copernicus

Atmosphere Monitoring Service (CAMS) reanalysis³⁰ as a proxy for wildfire aerosols (see Methods).

Black carbon AOD shows that wildfire emissions emanated mainly from south and eastern Australia and extended within a few days to the broad South Pacific between 20°S and 55°S (Fig. 1a, Extended Data Fig. 1 and Supplementary Video). Predominantly eastward aerosol transport is confirmed by air parcel forward trajectories initiated at the locations of wildfires (Extended Data Fig. 2). Emissions of black carbon aerosols were episodic. For example, the signal from January 8th, 2020, alone accounted for ~25% of the cumulative black carbon AOD for the whole month of January 2020. As AOD does not necessarily translate into deposition, we used the deposition fluxes estimated in the CAMS reanalysis and satellite chlorophyll a concentration ([Chla]) anomalies to define the oceanic regions with potential phytoplankton fertilization by aerosols from Australian 2019-2020 wildfires (see Methods for the model estimate of aerosol deposition and satellite [Chla] observations). By December 2019, [Chla] had increased by over 150% compared with monthly climatologies in large areas of the ocean. The surface area of the regions with [Chla] higher than the historical monthly maximum (>10 trillion m²) exceeded the size of Australia (Fig. 1d). We identified two regions, south of Australia and Pacific sector of the Southern Ocean, where [Chla] more than doubled compared with the climatological concentrations and atmospheric deposition exceeded 150 mg m⁻² in the 2019-2020 austral summer (Extended Data Fig. 3). In these two study regions (Fig. 1a and 1d), black carbon AOD reached values unprecedented in the 17-year aerosol reanalysis time series (at least 300% higher than their climatological values shown in Fig. 1b and 1c) and [Chla] reached concentrations never observed in a 22-year satellite time-series from ESA's Ocean Color Climate Change Initiative (Fig. 1e and 1f). While the forward air-parcel trajectories show the high [Chla] anomaly regions are in the path of the pyrogenic aerosol transport (Extended Data Fig. 2), we applied two different approaches to demonstrate the unprecedented nature of the [Chla] anomaly. First, we assessed the basin-wide response of [Chla] to the black carbon AOD anomaly (Extended Data Fig. 4), and second, we iteratively analyzed 4681 different 10x10 degree geographical domains in the South Pacific and Pacific sector of the Southern Ocean over the entire remotely sensed ocean color record (Extended Data Fig. 5). These analyses show that the [Chla] anomaly during the 2019-2020 Australian wildfires is unprecedented in the satellite record independently of how we define the study regions.

The [Chla] anomalies followed peaks in black carbon AOD with lag times on the order of days to weeks (Fig. 2). Earlier studies have explored the potential for dust to stimulate phytoplankton blooms and found similar relations between [Chla] and AOD^{26,32}. The anomalous phytoplankton blooms started around October 2019, peaked in January 2020 and lasted for over 4 months with regional differences (Fig. 2). The plankton blooms were independently confirmed by contemporaneous *in situ* measurements of particle concentrations from optical backscattering on biogeochemical (BGC) Argo floats, showing particle concentrations well above a climatology envelope during the bloom period (Fig. 3 and Extended Data Fig. 6, see Methods for BGC-Argo float measurements). Furthermore, [Chla] measured on the BGC-Argo floats confirmed that the observed particles were phytoplankton (Fig. 3), ruling out potential contamination of optical backscattering by aerosols (Supplementary Discussion). Most surprising is that the phytoplankton increase occurred in austral summer when a seasonal decline in [Chla] is normally observed (Fig. 1 and Extended Data Fig. 4). In these regions of the Southern Ocean, photosynthesis is generally limited by Fe in austral summer when light is sufficient and mixed layers are often shallower than

45 m^{21,33,34}. Therefore, additional Fe supply is required to support these anomalous phytoplankton blooms.

To evaluate the fertilization potential of the 2019-2020 Australian wildfire aerosols, we tracked wildfire emissions and transport in the atmosphere and measured Fe concentration in aerosols collected at a time-series station on the island of Tasmania, mostly downwind from the fire events in mainland Australia (see Methods). The total and labile concentrations of Fe (T_{Fe} and L_{Fe}) were substantially higher in fire-sourced samples compared with historical values (Extended Data Fig. 7). The highest total and labile concentrations of Fe ($T_{Fe}=257.4$ ng m⁻³ and $L_{Fe}=73.9$ ng m⁻³) were measured in aerosols between the 15th and 17th of January 2020. This sample also contained the highest concentration of levoglucosan (indicating the presence of biomass burning emissions in aerosols) and was collected while a large black carbon AOD plume travelled over the sampling location (Extended Data Fig. 8). Air parcel back trajectories confirm that the black carbon AOD plume originated from southeast Australia, the epicentre of the 2019-2020 Australian megafires (Extended Data Fig. 8). Wildfire-impacted aerosols showed significantly higher T_{Fe} ($p<0.05$, up to 5-fold increase) and L_{Fe} ($p<0.1$, up to 27-fold increase) concentrations compared with measurements at the same station between 2016 and 2019 (all seasons), including smaller and more localized wildfire events. This observation is consistent with other studies showing large atmospheric Fe input from pyrogenic sources¹³. The fraction of labile Fe was likely greater over our study region of the Pacific sector of the Southern Ocean as solubility is known to increase during atmospheric transport³⁵. Preliminary estimates show that Fe supply from aerosol deposition is sufficient to fulfill the Fe requirement to support the anomalous [Chla] increase (Supplementary Discussion). While Fe could have been supplied by other sources such as vertical mixing of Fe-rich water³⁶, we did not find a strong negative correlation between sea surface temperature and [Chla] anomalies in our study region and period (Supplementary Fig. 7). Overall, our analyses suggest that Fe-rich aerosols emanating from the 2019-2020 Australian wildfires were capable of fertilizing the observed expansive algal blooms in the Southern Ocean. While our study focuses on Fe, pyrogenic aerosols may also have contributed nutrients other than Fe^{8,9}, jointly stimulating phytoplankton response in the broad areas covered by elevated AOD plume (Fig. 1).

We evaluated the anomalous carbon export associated with phytoplankton blooms. Since AOD (and aerosol deposition) and phytoplankton productivity were enhanced in a larger portion of the South Pacific and Southern Ocean than the two selected regions in Fig. 1, we define a basin scale region of interest as the region with positive black carbon AOD anomalies (Extended Data Fig. 9). Satellite-estimated marine net primary production (NPP) and export production (EP) increased substantially during the 2019-2020 Australian wildfire season compared with the monthly climatologies (Fig. 4), corresponding to a cumulative net additional uptake of $\sim 186\pm 90$ Tg C from October 2019 to April 2020, equivalent to $\sim 95\pm 46\%$ of the CO₂ emission (~ 195 Tg C) from the 2019-2020 Australian wildfires. We refrain from providing an air-sea CO₂ flux associated with the anomalous carbon export because the ratio of cumulative air-sea CO₂ flux to carbon export associated with iron fertilization varies as a function of numerous factors and is highly uncertain³⁷ (Supplementary Discussion). We also note that the additional CO₂ uptake may not have been exported to the deep ocean, in which case the sequestration may be short-lived²¹. In addition, the responding phytoplankton groups remain to be determined, which could affect the carbon export efficiency. For example, the low silicic acid concentration in parts of the subantarctic zone may restrict the response of diatoms to Fe fertilization³⁸. The large-scale and long-term effects of the

2019-2020 Australian wildfires on primary production, carbon export and CO₂ exchange warrant further study.

Large-scale climate patterns influence ocean dynamics, nutrient supply and light regime, thereby modulating productivity and carbon uptake in the Southern Ocean³⁹. While the El Niño–Southern Oscillation (ENSO) index was neutral during the 2019-2020 Australian wildfires, the Indian Ocean Dipole (IOD) and Southern Annular Mode (SAM) were strongly positive and negative, respectively (Extended Data Fig. 10). However, [Chla] anomalies potentially driven by climate modes are substantially smaller (<10%) than what we observed during the 2019-2020 Australian wildfire season, as demonstrated by the predicted magnitude of the 2019-2020 excursion from the climatologies (Extended Data Fig. 10d and 10e). Climate patterns could also set the stage for conditions favorable to wildfires^{40,41}. Positive IOD and negative SAM are believed to precondition southeast Australia for wildfires by reducing rainfall and increasing temperature^{4,40}. Perhaps more significantly, the 2019-2020 summer in southeast Australia was also strongly driven towards hot and dry conditions by a stratospheric warming event⁴². Some Australian megafires have occurred during positive IOD and/or negative SAM events in the historical record (Extended Data Fig. 10). The frequency of extreme positive IOD is predicted to increase due to global warming, rendering southeastern Australia and eastern Asia more susceptible to wildfires⁴³. The impact on marine ecosystems downwind of these wildfires will likely depend on the wildfire intensity and duration, dispersal of pyrogenic aerosols, seasonal timing, and the ecosystem's initial state. A plankton ecosystem may not be responsive to Fe-rich aerosol deposition because of macronutrient or light limitation⁴⁴. Some of these factors may explain why not all Australian wildfires on record are associated with marine biological responses (Fig. 1 and Extended Data Fig. 10). Macronutrient limitation could also explain the lack of a strong [Chla] response in oligotrophic subtropical waters east of Australia despite being overlain with high black carbon AOD and aerosol deposition during the 2019-2020 Australian wildfires (Supplementary Discussion).

Modeling studies have highlighted the potential role of fire in providing bioavailable iron and other nutrients to downwind regions through atmospheric transport^{11,45}. Building on these studies, we provide observational evidence that aerosols originating from megafires contain sufficient iron to support a large phytoplankton response in the ocean. Human activity has altered nutrient supply and deposition to the ocean through local and global perturbations. Local perturbations such as land use change and fossil fuel burning enhance micro- and macronutrient mobilization and emission to the atmosphere^{45,46}. In turn, global perturbations to the water cycle and heat budget are leading to changes in wildfire and drought distributions, frequency and intensity¹⁴. There is increasing evidence that wildfires may have played an important role modulating atmospheric CO₂ during glacial-interglacial periods⁴⁷. They currently burn approximately 3% of the Earth's land annually, in the process emitting ~2.2 Pg C yr⁻¹ (CO₂)⁴⁸. Given the increasing risk of wildfires with climate change (e.g., in southeast Australia, the Amazon, and the western United States)¹⁻³, their central role in our global climate in the geological past, at present, and in our future therefore argues for a more comprehensive representation of wildfires in climate models. Among other things, extensive measurements of wildfire aerosols and targeted studies of their effects on marine ecosystems are needed to further elucidate the wide-ranging impacts, especially for an event of the magnitude of the 2019-2020 Australian wildfires.

References

- 1 Bowman, D. M. J. S. *et al.* Vegetation fires in the Anthropocene. *Nature Reviews Earth & Environment* **1**, 500-515 (2020).
- 2 Abatzoglou, J. T., Williams, A. P. & Barbero, R. Global Emergence of Anthropogenic Climate Change in Fire Weather Indices. *Geophysical Research Letters* **46**, 326-336 (2019).
- 3 Huang, Y., Wu, S. & Kaplan, J. O. Sensitivity of global wildfire occurrences to various factors in the context of global change. *Atmospheric Environment* **121**, 86-92 (2015).
- 4 van Oldenborgh, G. J. *et al.* Attribution of the Australian bushfire risk to anthropogenic climate change. *Nat. Hazards Earth Syst. Sci.* **21**, 941-960 (2021).
- 5 Ward, M. *et al.* Impact of 2019-2020 mega-fires on Australian fauna habitat. *Nat Ecol Evol* **4**, 1321-1326 (2020).
- 6 Kablick III, G. P., Allen, D. R., Fromm, M. D. & Nedoluha, G. E. Australian PyroCb Smoke Generates Synoptic-Scale Stratospheric Anticyclones. *Geophysical Research Letters* **47**, e2020GL088101 (2020).
- 7 Hirsch, E. & Koren, I. Record-breaking aerosol levels explained by smoke injection into the stratosphere. *Science* **371**, 1269-1274 (2021).
- 8 Schlosser, J. S. *et al.* Analysis of aerosol composition data for western United States wildfires between 2005 and 2015: Dust emissions, chloride depletion, and most enhanced aerosol constituents. *J Geophys Res Atmos* **122**, 8951-8966 (2017).
- 9 Barkley, A. E. *et al.* African biomass burning is a substantial source of phosphorus deposition to the Amazon, Tropical Atlantic Ocean, and Southern Ocean. *Proceedings of the National Academy of Sciences* **116**, 16216-16221 (2019).
- 10 Guieu, C., Bonnet, S., Wagener, T. & Loÿe-Pilot, M.-D. Biomass burning as a source of dissolved iron to the open ocean? *Geophysical Research Letters* **32**, L19608 (2005).
- 11 Ito, A. Mega fire emissions in Siberia: potential supply of bioavailable iron from forests to the ocean. *Biogeosciences* **8**, 1679-1697 (2011).
- 12 Abram, N. J., Gagan, M. K., McCulloch, M. T., Chappell, J. & Hantoro, W. S. Coral Reef Death During the 1997 Indian Ocean Dipole Linked to Indonesian Wildfires. *Science* **301**, 952-955 (2003).
- 13 Ito, A. *et al.* Pyrogenic iron: The missing link to high iron solubility in aerosols. *Science Advances* **5**, eaau7671 (2019).
- 14 Jia, G. *et al.* Land-climate interactions in *Climate Change and Land: an IPCC special report on climate change, desertification, land degradation, sustainable land management, food security, and greenhouse gas fluxes in terrestrial ecosystems*. In press.
- 15 Jiang, Y. *et al.* Impacts of Wildfire Aerosols on Global Energy Budget and Climate: The Role of Climate Feedbacks. *Journal of Climate* **33**, 3351-3366 (2020).
- 16 Bowman, D. *et al.* Wildfires: Australia needs national monitoring agency. *Nature* **584**, 188-191 (2020).
- 17 New WWF report: 3 billion animals impacted by Australia's bushfire crisis. <https://www.wwf.org.au/news/news/2020/3-billion-animals-impacted-by-australia-bushfire-crisis#gs.ebzve2> (2020).
- 18 van der Velde, I. R. *et al.* Vast CO₂ release from Australian fires in 2019-2020 constrained by satellite. *Nature*. In review.
- 19 National Greenhouse Gas Inventory Report: 2018. <https://www.industry.gov.au/data-and-publications/national-greenhouse-gas-inventory-report-2018> (2020).

- 20 Mahowald, N. M. *et al.* Aerosol impacts on climate and biogeochemistry. *Annual Review of Environment and Resources* **36**, 45-74 (2011).
- 21 Boyd, P. W. *et al.* Mesoscale iron enrichment experiments 1993-2005: Synthesis and future directions. *Science* **315**, 612-617 (2007).
- 22 Jickells, T. *et al.* Global iron connections between desert dust, ocean biogeochemistry, and climate. *Science* **308**, 67-71 (2005).
- 23 Martin, J. H. Glacial-interglacial CO₂ change: The iron hypothesis. *Paleoceanography* **5**, 1-13 (1990).
- 24 Tagliabue, A. *et al.* Surface-water iron supplies in the Southern Ocean sustained by deep winter mixing. *Nature Geoscience* **7**, 314-320 (2014).
- 25 Cassar, N. *et al.* The Southern Ocean biological response to aeolian iron deposition. *Science* **317**, 1067-1070 (2007).
- 26 Gabric, A. J., Cropp, R., Ayers, G. P., McTainsh, G. & Braddock, R. Coupling between cycles of phytoplankton biomass and aerosol optical depth as derived from SeaWiFS time series in the Subantarctic Southern Ocean. *Geophysical Research Letters* **29**, 16-11-16-14 (2002).
- 27 Ardyna, M. *et al.* Hydrothermal vents trigger massive phytoplankton blooms in the Southern Ocean. *Nat Commun* **10**, 2451 (2019).
- 28 Duprat, L. P. A. M., Bigg, G. R. & Wilton, D. J. Enhanced Southern Ocean marine productivity due to fertilization by giant icebergs. *Nature Geosci* **9**, 219-221 (2016).
- 29 Bixby, R. J. *et al.* Fire effects on aquatic ecosystems: an assessment of the current state of the science. *Freshwater Science* **34**, 1340-1350 (2015).
- 30 Inness, A. *et al.* The CAMS reanalysis of atmospheric composition. *Atmos. Chem. Phys.* **19**, 3515-3556 (2019).
- 31 Orsi, A. H., Whitworth, T. & Nowlin, W. D. On the meridional extent and fronts of the Antarctic Circumpolar Current. *Deep Sea Research Part I: Oceanographic Research Papers* **42**, 641-673 (1995).
- 32 Shafeeque, M., Sathyendranath, S., George, G., Balchand, A. N. & Platt, T. Comparison of Seasonal Cycles of Phytoplankton Chlorophyll, Aerosols, Winds and Sea-Surface Temperature off Somalia. *Frontiers in Marine Science* **4**, 384 (2017).
- 33 Cassar, N. *et al.* The influence of iron and light on net community production in the Subantarctic and Polar Frontal Zones. *Biogeosciences* **8**, 227-237 (2011).
- 34 Mitchell, B. G. & Holm-Hansen, O. Observations of modeling of the Antarctic phytoplankton crop in relation to mixing depth. *Deep Sea Research Part A. Oceanographic Research Papers* **38**, 981-1007 (1991).
- 35 Longo, A. F. *et al.* Influence of Atmospheric Processes on the Solubility and Composition of Iron in Saharan Dust. *Environmental science & technology* **50**, 6912-6920 (2016).
- 36 Meskhidze, N., Nenes, A., Chameides, W. L., Luo, C. & Mahowald, N. Atlantic Southern Ocean productivity: Fertilization from above or below? *Global Biogeochemical Cycles* **21**, GB2006 (2007).
- 37 Sarmiento, J. L., Slater, R. D., Dunne, J., Gnanadesikan, A. & Hiscock, M. R. Efficiency of small scale carbon mitigation by patch iron fertilization. *Biogeosciences* **7**, 3593-3624 (2010).

- 38 Brzezinski, M. A., Jones, J. L. & Demarest, M. S. Control of silica production by iron and silicic acid during the Southern Ocean Iron Experiment (SOFeX). *Limnology and Oceanography* **50**, 810-824 (2005).
- 39 Lovenduski, N. S. & Gruber, N. Impact of the Southern Annular Mode on Southern Ocean circulation and biology. *Geophysical Research Letters* **32**, L11603 (2005).
- 40 Cai, W., Cowan, T. & Raupach, M. Positive Indian Ocean Dipole events precondition southeast Australia bushfires. *Geophysical Research Letters* **36**, L19710 (2009).
- 41 Chen, Y. *et al.* A pan-tropical cascade of fire driven by El Niño/Southern Oscillation. *Nature Climate Change* **7**, 906-911 (2017).
- 42 Lim, E.-P. *et al.* Australian hot and dry extremes induced by weakenings of the stratospheric polar vortex. *Nature Geoscience* **12**, 896-901 (2019).
- 43 Cai, W. *et al.* Increased frequency of extreme Indian Ocean Dipole events due to greenhouse warming. *Nature* **510**, 254-258 (2014).
- 44 Cropp, R. A. *et al.* The likelihood of observing dust-stimulated phytoplankton growth in waters proximal to the Australian continent. *Journal of Marine Systems* **117-118**, 43-52 (2013).
- 45 Hamilton, D. S. *et al.* Impact of Changes to the Atmospheric Soluble Iron Deposition Flux on Ocean Biogeochemical Cycles in the Anthropocene. *Global Biogeochemical Cycles* **34**, e2019GB006448 (2020).
- 46 Duce, R. *et al.* Impacts of atmospheric anthropogenic nitrogen on the open ocean. *Science* **320**, 893-897 (2008).
- 47 Han, Y. *et al.* Asian inland wildfires driven by glacial-interglacial climate change. *Proceedings of the National Academy of Sciences of the United States of America* **117**, 5184-5189 (2020).
- 48 van der Werf, G. R. *et al.* Global fire emissions estimates during 1997–2016. *Earth System Science Data* **9**, 697-720 (2017).

Fig. 1 | Maps of black carbon AOD and [Chla] anomalies and their historical records. (a) Cumulative black carbon AOD anomaly for the 2019-2020 austral summer. (b) Daily time-series of black carbon AOD for waters south of Australia (solid black box in panels a and d). (c) Daily time-series of black carbon AOD in the Pacific Southern Ocean (solid black box in panels a and d). (d) [Chla] relative anomaly for the 2019-2020 austral summer. The dashed box within the ‘Pacific Southern Ocean’ box is used to show temporal variations of black carbon AOD and [Chla] time-series during the 2019-2020 Australian wildfires in Fig. 2. (e) Monthly time-series of [Chla] in waters south of Australia (solid black line). Monthly climatological values shown in dotted black line. Red and cyan areas denote monthly data higher or lower than climatological values, respectively. (f) Monthly time-series of [Chla] in the Pacific subantarctic Southern Ocean (south of the subtropical front). Dotted, dot-dashed, and solid black lines in a and d represent the climatological positions of the subtropical front, subantarctic front and polar front, respectively³¹.

Fig. 2. | Temporal patterns of black carbon AOD and satellite [Chla] in two regions denoted in Fig. 1 during the 2019-2020 Australian wildfire season. (a) Waters south of Australia and (b) Pacific Southern Ocean (south of the subtropical front). Daily black carbon AOD is shown in vertical bars. Solid and dashed green lines represent the 8-day mean [Chla] for 2019-2020 and climatological records, respectively. Green shaded areas indicate ± 1 standard deviation. The

episodic aerosol transport events are illustrated by the sharp peaks of black carbon AOD while the biological responses are sustained for a longer period.

Fig. 3. | Plankton blooms observed by *in situ* measurements from BGC-Argo floats and satellites. (a) Comparison between *in situ* summer 2019-2020 particulate backscatter (b_{bp} , solid lines) measured by three BGC-Argo floats and the corresponding satellite climatology (dotted lines, standard deviation shown as envelope). Float trajectories are displayed on the inset map in subplot **b** (line and trajectory colors correspond). Float b_{bp} was calibrated to satellite b_{bp} (see Methods for details). Error bars indicate the uncertainty introduced by the calibration. Climatological b_{bp} values were calculated individually from satellite b_{bp} for each profile location. (b) *In situ* [Chla] measured by the three BGC-Argo floats. Float positions from September 2019 through March 2020 are highlighted (traveling mostly from west to east during the fire season). Float IDs specified in the key. (c) Satellite [Chla] average over two sub-regions encompassing the float paths.

Fig. 4. | Enhancement in marine phytoplankton productivity during the 2019-2020 Australian wildfires. (a) Satellite-estimated monthly net primary production (NPP) and (b) export production (EP) during 2019-2020 Australian wildfire season (orange bars) compared with their monthly climatologies (blue bars) at the basin scale (20°S-55°S, 120°E-90°W) (Extended Data Fig. 9). Error bars represent one standard deviation of monthly NPP or EP from 2003 to 2018 (for climatology) and from 2019 October to 2020 April (for wildfire season) derived from 3 NPP and 9 EP model estimates. The total anomalous NPP and EP were 753 ± 300 Tg C and 186 ± 90 Tg C respectively from 2019 October to 2020 April.

Methods

Satellite chlorophyll-a observations

The ocean-color satellite record of chlorophyll-a ([Chla]) used in this study is a merged multi-sensor record spanning 22 years and was created by the OC-CCI project⁴⁹. The exact product was the v4.2 weekly chlorophyll-a composite data that includes updates for the latest NASA reprocessing (R2018). The dataset is created by band-shifting and bias-correcting MERIS, MODIS and VIIRS reflectance data to match SeaWiFS data, merging the datasets and computing per-pixel uncertainty estimates. The chlorophyll-a products are then calculated from the merged ocean color remote-sensing reflectance record. More details on data production and access can be found at <http://www.esa-oceancolour-cci.org/>.

Aerosol reanalysis and deposition

The Aerosol Optical Depth (AOD) and deposition fluxes used in this study are extracted from the Copernicus Atmosphere Monitoring Service (<http://atmosphere.copernicus.eu>, CAMS), which is a component of the European Earth observation programme Copernicus (<https://www.copernicus.eu/en>) produced by the European Centre for Medium-Range Weather Forecasts (ECMWF). CAMS produces global reanalysis data sets of reactive trace gases, greenhouse gases and aerosol concentrations³⁰. The CAMS reanalysis consists of 3-dimensional time-consistent atmospheric composition fields, including aerosols and chemical species delivered at a frequency of 3-6 hours, yet subsampled at a daily frequency for this study. The CAMS aerosol model component is based on the Integrated Forecasting System (IFS) meteorological model⁵⁰ and

contains 12 prognostic tracers: three size-bins of sea salt, three more for dust, hydrophilic and hydrophobic Black-Carbon (BC) and Organic Matter (OM), plus sulfate aerosol and a gas-phase sulfur dioxide (SO₂) precursor³⁰. CAMS aerosols are assimilated with satellite observations (MODIS)⁵¹ of total AOD at 550 nm. As the aerosol model contains more aerosol components than what can be estimated from AOD satellite observations, the sum of the aerosol species is used as control variable and repartitioned into individual aerosol components according to their fractional contribution to the total aerosol mass⁵². The sources of BC are derived from the Global Fire Assimilation System (GFASv1.2)⁵³ scaled up with a geographically varying but temporally constant factor³⁰. GFASv1.2 estimates near-real-time emissions based on the satellite-observed fire radiative power.

CAMS is a state-of-the-art atmospheric reanalysis that performs well in reproducing observed total AOD and fire-related components such as carbon monoxide (CO) and nitrogen dioxide (NO₂)⁵⁴. The lack of field measurements that disentangle black carbon AOD from the total AOD, and the difficulty of acquiring field measurements of atmospheric deposition fluxes, particularly for wet deposition in the Southern Hemisphere⁵⁵, preclude a direct validation of CAMS performance on these variables. However, given the exceptional emission of BC during the Australian 2019-2020 fire season⁵⁶, the uncertainty in the amount of BC in the total AOD estimated from the assimilation is not expected to impact the patterns and variability of black carbon AOD shown in this study.

BGC-Argo float observations

In situ particulate backscatter (b_{bp}) measurements as a proxy for phytoplankton biomass, taken by autonomous biogeochemical (BGC) Argo profiling floats, were used to corroborate the phytoplankton blooms highlighted by the satellite analyses. [Chla] observed by floats were also provided for comparison. We focus on b_{bp} rather than [Chla] because there are fewer confounding factors for b_{bp} when relating satellite to float data. Satellite [Chla] is based on absorption, whereas float [Chl-a] is based on fluorescence and affected by non-photochemical quenching and calibration uncertainties. Combining satellite and float b_{bp} observations allowed us to create a satellite climatology of b_{bp} with which to compare the float b_{bp} . The raw float data used here are openly accessible on the Ifremer ftp-server (<ftp://ftp.ifremer.fr/ifremer/argo/dac/>). Three floats from the Pacific Southern Ocean (float IDs: 5904685, 5904842, 5904843) were selected for the analysis, based on their sampling of the bloom areas identified in the satellite data during 2019-2020 (Fig. 1, float trajectories in Fig. 3). The floats profiled from 2000 m to the surface every 10 days.

Float and satellite b_{bp} were matched in three steps. First, float b_{bp} at 700 nm wavelength was converted to b_{bp} at 443 nm, the wavelength measured by MODIS Aqua, assuming a spectrally invariant particular backscattering ratio and using the relationship $b_{bp}(443) = b_{bp}(700) \left(\frac{443}{700}\right)^{-\gamma}$, where $\gamma = 0.78$ (57,58). Secondly, from the depth-resolved float b_{bp} , surface b_{bp} estimates at each profile location were then calculated as the median b_{bp} between 0 and 20m depth. Finally, float surface b_{bp} was calibrated to MODIS Aqua, 8-day, 4 km satellite surface $b_{bp}(443)$ using model II linear regressions (Extended Data Fig. 6). Calibrations were performed individually for each float and were based on the entire b_{bp} dataset gathered during each float's lifetime. To minimize cloud coverage and maximize data availability, satellite values were averaged in time and space in two different ways: 16-day/60x60 km averages and 24-day/20x20 km averages. Spatial averages were centered around each profile location. Temporal averages were calculated from two or three

consecutive MODIS Aqua 8-day intervals closest to the profile date. The uncertainty introduced by the calibration $b_{bp,cal} = b_{bp} \cdot a + b$, where a and b are slope and intercept of the regression, was propagated using the regression coefficients' standard deviations: $\sigma b_{bp,cal} = \sqrt{(b_{bp} \cdot \sigma a)^2 + \sigma b^2}$, where σ denotes the standard deviation.

For each 2019-2020 b_{bp} value, a climatological counterpart was calculated by averaging the respective MODIS Aqua 8-day interval from 2002 to 2018 over a 60x60km area centered around the profile location. To reduce the impact of cloud noise on the calibration, b_{bp} match-ups were excluded where the satellite average's relative standard deviation exceeded 10%. The uncertainty of each climatological value is equal to the standard deviation of all b_{bp} values averaged.

Mixed layer depth from Argo floats

Mixed layer depth (MLD) was calculated from the temperature and salinity profiles of Argo floats in the Southern Ocean. Argo floats data were downloaded from <https://nrlgodae1.nrlmry.navy.mil>, and were filtered by retaining profiles marked with a quality flag of '1' ('good data') or '2' ('probably good data'). The filtered profiles were used to calculate MLD which is defined as the depth at which the potential density exceeds a near-surface (10 m) reference value by 0.03 kg m^{-3} ^(59,60). The MLD estimates were averaged to obtain monthly resolution in 2° by 2° spatial grids.

Aerosol iron sampling and analysis

The Mount Wellington aerosol time-series sampling station is located at an elevation of 1271 m above sea level, on the top of Mount Wellington / kunanyi in southern Tasmania, Australia (coordinates: 42.89°S , 147.24°E). Total suspended aerosol particles were collected on acid-washed Whatman 41 cellulose filter paper^{61,62} using a high-volume air sampler HiVol 3000 (Ecotech, Rhode Island, USA). Samples used for this study were collected between the 17th December 2019 and the 11th February 2020 while wildfires were raging in mainland Australia. Samples were collected over 3-day to 2-week periods and stored frozen at the Institute for Marine and Antarctic Studies (Hobart, Tasmania, Australia) prior to analysis. To highlight the impact of the unprecedented fire emissions on aerosol characteristics downwind of the wildfires, aerosol concentrations (total and labile Fe) during the 2019-2020 fire season were compared to measurements made at the same time-series station between October 2016 and December 2019 (mostly from late October to early April annually due to logistic difficulties sampling over winter).

Aerosol Fe concentrations were assessed using a 3-step leaching protocol⁶³. Sample handling was carried out in an HEPA-filtered laminar flow hood in a positive pressured class 6 clean room, following GEOTRACES procedures⁶¹. Aerosol samples were successively extracted using an instantaneous flow-through leach of ultra-high purity water, followed by a one-hour batch leach using a pH 4.7 ammonium acetate buffer solution. Fe concentrations measured in the two leaches were summed to obtain the labile Fe content in aerosols, which is interpreted as an estimate for the bioavailable fraction for marine phytoplankton growth following atmospheric deposition^{63,64}. The remaining filter was digested using a mixture of hydrofluoric and nitric acids at 120°C for 12h. The sum of the three leaches defines the total Fe concentration in the aerosols. All analyses were undertaken using Sector Field Inductively Coupled Plasma-Mass Spectrometry (SF-ICP-MS, Thermo Fisher Scientific ELEMENT 2; full details in Perron et al. (2020)⁶³).

The total Fe concentration measured in aerosols averaged 57.1 ng m^{-3} (median 43.5 ng m^{-3}) before the fire season and increased to 97.2 ng m^{-3} (median 76.6 ng m^{-3}) between December 17th, 2019, and February 11th, 2020, while wildfires were raging in mainland Australia. The concentration of labile Fe averaged 12.5 ng m^{-3} (median 5.1 ng m^{-3}) over the study period, which exceeds the average labile Fe of 3.5 ng m^{-3} (median 2.7 ng m^{-3}) measured at this sampling site prior the 2019-2020 fire period while smaller bushfires and anthropogenic emissions prevailed. A T-test (preceded by a variance F-test) was conducted and showed that both total and labile Fe concentrations are statistically different than the historical values ($p < 0.05$ and $p < 0.1$, respectively in Supplementary Table 1). A greater significance level is acceptable for the labile Fe concentration as this parameter varies highly according to the dominant atmospheric source in aerosols. Indeed, anthropogenic emissions included in aerosols from the time series (prior the fire period) are known to enhance Fe solubility leading to high labile Fe concentration in aerosols.

Chemical tracers were used to differentiate aerosols collected between December 2019 and February 2020 that are only affected by the Australian wildfires and aerosols containing other atmospheric sources. Levoglucosan, a monosaccharide anhydride formed during the pyrolysis of cellulose, served as an intrinsic indicator for biomass burning in aerosols collected during the 2019-2020 Australian wildfire events. Levoglucosan quantitation was carried out by ion chromatography tandem mass spectrometry (IC-MS/MS)⁶⁵. Briefly, a subset of aerosol filter was extracted using 6 mL of deionized water in an ultrasonic bath for 20 min at 20°C, filtered and analyzed using a Thermo Scientific™ Dionex™ ICS-5000⁺ Reagent-Free™ IC (RFIC™) system coupled to a Thermo Scientific™ TSQ Quantiva™ triple-stage quadrupole mass spectrometer. As the atmospheric concentration of levoglucosan varies according to the source and location (distance travelled) of the detected fire, this tracer was only used as a qualitative tool in aerosols. In addition, lead and copper were chosen as indicators of anthropogenic emissions in aerosols as the two metals mainly originate from fuel combustion sources. A significant impact from human-derived emissions on aerosol samples was stated when both enrichment factors (elemental ratio to aluminum compared to the same ratio in the averaged upper continental crust⁶⁶) in lead and copper exceeded the commonly chosen threshold of 10⁽⁶⁷⁾. Anthropogenic pollution is known to enhance the fraction of labile Fe in aerosols⁶⁸. Aerosols samples collected during the 2019-2020 peak fire season contained levoglucosan concentrations between 0.26 ng m^{-3} and 283.36 ng m^{-3} , and showed no evidence of anthropogenic contamination.

Atmospheric trajectory analysis

Forward air parcel trajectories were applied to track the transport of aerosols emitted from 2019-2020 Australian wildfires while back trajectories were used to determine the origins of aerosols collected at the aerosol time-series station in Tasmania. These trajectory analyses were performed using the Hybrid Single-Particle Lagrangian Integrated Trajectory model (HYSPLIT)⁶⁹. We used meteorological data acquired from NCEP/NCAR Reanalysis⁷⁰ spanning the period from November 2019 to March 2020 (<https://www.ready.noaa.gov/archives.php>). For the forward trajectories, we analyzed some major fire events in the southeastern Australia, e.g., starting on 26 October 2019 in Gospers Mountain, North South Wales (33°S, 150.4°E), on 26 November 2019 in Shoalhaven, North South Wales (35.5°S, 150.5°E) and on 26 December 2019 in the Sterling Ranges, Western Australia (34.4°S, 118°E) (<https://www.createdigital.org.au/australian-bushfires-a-timeline-of-whats-happened-so-far/> and <https://www.nsw.gov.au/nsw-government/projects-and-initiatives/nsw-bushfire-inquiry>). The coordinates correspond to the

approximate locations of these fires. The model was initiated at 00 UTC and 500 m above ground level for each source region and date to calculate forward trajectories of 168 hours (7 days), with a new trajectory launched every 6 hours for a duration of 10 days. These parameters are commonly used in previous studies to map the aerosol transport in the atmosphere⁷¹. In addition, we used these locations to estimate the aerosol emission and transport over the majority of the fire season, i.e., trajectories were launched daily and were run from November 2019 to January 2020. The forward trajectories extended mainly around Australia and toward the Pacific Southern Ocean as shown in Extended Data Fig. 2. Air parcel trajectories and wildfire aerosol plumes don't always coincide because of uncertainties in parameters used in the trajectory analysis, e.g., the timing and locations of the fires, and the variation in heights that aerosol could reach⁷² (Supplementary Discussion).

For the back trajectories, we traced the sources of aerosols collected at the aerosol time-series station in Tasmania. For example, the highest Fe concentration was observed for aerosols collected from 15 January 2020 to 17 January 2020. The model was initiated at 00 UTC 17 January 2020 and at the station location (1271 m above sea level, 42.89°S, 147.24°E) to calculate back trajectories of 120 hours (5 days), with a new trajectory launched every 6 hours. Air parcels preferentially originated from the southeastern mainland Australia where wildfires were occurring as shown in Extended Data Fig. 8. Overall, trajectory analysis corroborates the emission and transport of aerosols as seen from the satellite-observed and reanalyzed aerosol optical depth (AOD).

Primary production and export production estimates

We estimate the enhancement in marine phytoplankton productivity at the basin scale (20°S-55°S, 120°E-90°W) during the 2019-2020 Australian wildfires shown in Extended Data Fig. 9. Monthly net primary production (NPP) was calculated based on the vertically generalized production model (VGPM)⁷³, carbon-based production model (CbPM)^{74,75}, and carbon, absorption, and fluorescence euphotic-resolving model (CAFE)⁷⁶ using MODIS satellite observations of monthly chlorophyll a concentration ([Chla]), photosynthetically available radiation (PAR), MLD, nitracline, inherent optical properties (IOPs), and sea surface temperature (SST) (<https://oceancolor.gsfc.nasa.gov/> and <http://sites.science.oregonstate.edu/ocean.productivity/index.php>). Export production (EP) was determined via multiplying NPP by an export ratio. Three different export ratios⁷⁷⁻⁷⁹ were separately applied to each NPP model: 1. $ef = 0.04756 \times \left(0.78 - \frac{0.43 \times SST}{30} \times NPP^{0.307}\right)$; 2. $ef = -0.0081 \times SST + 0.0806 \times \ln([Chla]) + 0.426$; 3. $ef = \frac{8.57}{17.9 + SST}$. Monthly export production was calculated as the mean of the 9 estimates. The monthly NPP and EP anomalies were reflected in the differences of monthly NPP and EP during the 2019-2020 wildfire season in comparison to their respective monthly climatologies. We finally integrated the differences from October 2019 to April 2020 to calculate the total additional biological CO₂ uptake and export. Uncertainties associated with different algorithms to calculate NPP and export ratio in the ocean are presented in earlier studies^{79,80}. We provide the anomalous NPP and EP estimated from each model in the Supplementary Table 2.

Since SST is an important factor in determining the export ratio, we have also applied climatological SST to decipher the contribution of SST anomalies to the enhancement in carbon export (Supplementary Fig. 8). Because of the small and heterogenous SST anomalies, the

contribution of SST anomalies to carbon export is negligible compared to the widespread increase in [Chla] or NPP.

Chlorophyll-a anomalies driven by climate variabilities

We evaluated the potential influence of southern annular mode (SAM) and Indian ocean dipole (IOD) on the observed anomalies of [Chla] during the 2019-2020 wildfire season. Two linear regression models were developed by using monthly [Chla] anomalies (after removing seasonality) as predictand and using monthly SAM or IOD indices as the predictors for the period 2003-2018 following the method in Lovenduski & Gruber, 2005⁽³⁹⁾. The monthly SAM⁸¹ and IOD⁸² indices were obtained from <https://climatedataguide.ucar.edu/climate-data/marshall-southern-annular-mode-sam-index-station-based> and https://psl.noaa.gov/gcos_wgsp/Timeseries/DMI/, respectively. The regression models were applied to individual climate indices from December 2019 to February 2020 to predict their impact on monthly [Chla] anomalies. The predicted anomalies are substantially smaller than the observed [Chla] anomalies (Extended Data Fig. 10).

- 49 Sathyendranath, S. *et al.* An Ocean-Colour Time Series for Use in Climate Studies: The Experience of the Ocean-Colour Climate Change Initiative (OC-CCI). *Sensors* **19**, 4285 (2019).
- 50 Morcrette, J.-J. *et al.* Aerosol analysis and forecast in the European Centre for Medium-Range Weather Forecasts Integrated Forecast System: Forward modeling. *Journal of Geophysical Research: Atmospheres* **114**, D06206 (2009).
- 51 Levy, R. C. *et al.* Exploring systematic offsets between aerosol products from the two MODIS sensors. *Atmos Meas Tech* **11**, 4073-4092 (2018).
- 52 Benedetti, A. *et al.* Aerosol analysis and forecast in the European Centre for Medium-Range Weather Forecasts Integrated Forecast System: 2. Data assimilation. *Journal of Geophysical Research* **114**, D13 (2009).
- 53 Kaiser, J. W. *et al.* Biomass burning emissions estimated with a global fire assimilation system based on observed fire radiative power. *Biogeosciences* **9**, 527-554 (2012).
- 54 Y. Bennouna *et al.* Validation report of the CAMS global reanalysis of aerosols and reactive gases, years 2003–2019. *Copernicus Atmosphere Monitoring Service (CAMS) report* (2020).
- 55 Ito, A. *et al.* Evaluation of aerosol iron solubility over Australian coastal regions based on inverse modeling: implications of bushfires on bioaccessible iron concentrations in the Southern Hemisphere. *Progress in Earth and Planetary Science* **7**, 42 (2020).
- 56 Khaykin, S. *et al.* The 2019/20 Australian wildfires generated a persistent smoke-charged vortex rising up to 35 km altitude. *Communications Earth & Environment* **1**, 22 (2020).
- 57 Haëntjens, N., Boss, E. & Talley, L. D. Revisiting Ocean Color algorithms for chlorophyll a and particulate organic carbon in the Southern Ocean using biogeochemical floats. *Journal of Geophysical Research: Oceans* **122**, 6583-6593 (2017).
- 58 Boss, E. *et al.* The characteristics of particulate absorption, scattering and attenuation coefficients in the surface ocean; Contribution of the Tara Oceans expedition. *Methods in Oceanography* **7**, 52-62 (2013).
- 59 de Boyer Montégut, C., Madec, G., Fischer, A. S., Lazar, A. & Iudicone, D. Mixed layer depth over the global ocean: An examination of profile data and a profile-based climatology. *Journal of Geophysical Research: Oceans* **109**, C12003 (2004).

- 60 Dong, S., Sprintall, J., Gille, S. T. & Talley, L. Southern Ocean mixed-layer depth from
Argo float profiles. *Journal of Geophysical Research: Oceans* **113**, C06013 (2008).
- 61 Cutter, G. A. *et al.* Sampling and Sample-handling Protocols for GEOTRACES Cruises,
Version 3.0. (2017).
- 62 Morton, P. L. *et al.* Methods for the sampling and analysis of marine aerosols: results
from the 2008 GEOTRACES aerosol intercalibration experiment. *Limnology and
Oceanography: Methods* **11**, 62-78 (2013).
- 63 Perron, M. M. G. *et al.* Assessment of leaching protocols to determine the solubility of
trace metals in aerosols. *Talanta* **208**, 120377 (2020).
- 64 Shelley, R. U., Landing, W. M., Ussher, S. J., Planquette, H. & Sarthou, G. Regional
trends in the fractional solubility of Fe and other metals from North Atlantic aerosols
(GEOTRACES cruises GA01 and GA03) following a two-stage leach. *Biogeosciences*
15, 2271-2288 (2018).
- 65 Sanz Rodriguez, E. *et al.* Analysis of levoglucosan and its isomers in atmospheric
samples by ion chromatography with electrospray lithium cationisation - Triple
quadrupole tandem mass spectrometry. *J Chromatogr A* **1610**, 460557 (2020).
- 66 McLennan, S. M. Relationships between the trace element composition of sedimentary
rocks and upper continental crust. *Geochemistry, Geophysics, Geosystems* **2**, 1201
(2001).
- 67 Shelley, R. U. *et al.* Quantification of trace element atmospheric deposition fluxes to the
Atlantic Ocean (>40°N; GEOVIDE, GEOTRACES GA01) during spring 2014. *Deep Sea
Research Part I: Oceanographic Research Papers* **119**, 34-49 (2017).
- 68 Sholkovitz, E. R., Sedwick, P. N., Church, T. M., Baker, A. R. & Powell, C. F. Fractional
solubility of aerosol iron: Synthesis of a global-scale data set. *Geochimica et
Cosmochimica Acta* **89**, 173-189 (2012).
- 69 Stein, A. F. *et al.* NOAA's HYSPLIT Atmospheric Transport and Dispersion Modeling
System. *Bulletin of the American Meteorological Society* **96**, 2059-2077 (2016).
- 70 Kalnay, E. *et al.* The NCEP/NCAR 40-year reanalysis project. *Bulletin of the American
meteorological Society* **77**, 437-471 (1996).
- 71 Tathego, M., Bhattachan, A., Okin, G. S. & D'Odorico, P. Mapping Areas of the
Southern Ocean Where Productivity Likely Depends on Dust-Delivered Iron. *Journal of
Geophysical Research: Atmospheres* **125**, e2019JD030926 (2020).
- 72 Stein, A. F., Rolph, G. D., Draxler, R. R., Stunder, B. & Ruminski, M. Verification of the
NOAA Smoke Forecasting System: Model Sensitivity to the Injection Height. *Weather
and Forecasting* **24**, 379-394 (2009).
- 73 Behrenfeld, M. J. & Falkowski, P. G. Photosynthetic rates derived from satellite-based
chlorophyll concentration. *Limnology and oceanography* **42**, 1-20 (1997).
- 74 Behrenfeld, M. J., Boss, E., Siegel, D. A. & Shea, D. M. Carbon-based ocean
productivity and phytoplankton physiology from space. *Global Biogeochemical Cycles*
19, GB1006 (2005).
- 75 Westberry, T., Behrenfeld, M. J., Siegel, D. A. & Boss, E. Carbon-based primary
productivity modeling with vertically resolved photoacclimation. *Global Biogeochemical
Cycles* **22**, GB2024 (2008).
- 76 Silsbe, G. M., Behrenfeld, M. J., Halsey, K. H., Milligan, A. J. & Westberry, T. K. The
CAFE model: A net production model for global ocean phytoplankton. *Global
Biogeochemical Cycles* **30**, 1756-1777 (2016).

- 77 Laws, E. A., D'Sa, E. & Naik, P. Simple equations to estimate ratios of new or export production to total production from satellite-derived estimates of sea surface temperature and primary production. *Limnology and Oceanography: Methods* **9**, 593-601 (2011).
- 78 Dunne, J. P., Armstrong, R. A., Gnanadesikan, A. & Sarmiento, J. L. Empirical and mechanistic models for the particle export ratio. *Global Biogeochemical Cycles* **19**, GB4026 (2005).
- 79 Li, Z. & Cassar, N. Satellite estimates of net community production based on O₂/Ar observations and comparison to other estimates. *Global Biogeochemical Cycles* **30**, 735-752 (2016).
- 80 Siegel, D. A. *et al.* Global assessment of ocean carbon export by combining satellite observations and food-web models. *Global Biogeochemical Cycles* **28**, 181-196 (2014).
- 81 Marshall, G. J. Trends in the Southern Annular Mode from Observations and Reanalyses. *Journal of Climate* **16**, 4134-4143 (2003).
- 82 Saji, N. H. & Yamagata, T. Possible impacts of Indian Ocean Dipole mode events on global climate. *Climate Research* **25**, 151-169 (2003).

Data Availability

The ESA's chlorophyll-a products can be accessed at <http://www.esa-oceancolour-cci.org/>. Satellite aerosol data are available from the Giovanni online data system (<https://giovanni.gsfc.nasa.gov/giovanni/>). The Copernicus Atmosphere Monitoring Service (CAMS) aerosol reanalysis datasets can be downloaded from the CAMS Atmosphere Data Store (ADS; <https://ads.atmosphere.copernicus.eu/cdsapp#!/dataset/cams-global-reanalysis-eac4?tab=overview>). The Argo float data are openly available on the Ifremer ftp-server (<ftp://ftp.ifremer.fr/ifremer/argo/dac/>). The net primary production estimates are available from Ocean Productivity website (<http://sites.science.oregonstate.edu/ocean.productivity/index.php>). Access to datasets analyzed in this study are also provided in the Methods section. Datasets generated in this study are provided as Source data and at <http://doi.org/10.5281/zenodo.4895657>.

Acknowledgements

Analyses of satellite aerosol observations used in this study were produced with the Giovanni online data system, developed and maintained by the NASA GES DISC. We would like to thank MODIS mission scientists and associated NASA personnel for the production of the data used in this research effort. The BGC-Argo data were collected and made freely available by the International Argo Program and the national programs that contribute to it (<http://www.argo.ucsd.edu>, <http://argo.jcommops.org>). The Argo Program is part of the Global Ocean Observing System (<https://doi.org/10.17882/42182>). Weiyi Tang is supported by the Harry H. Hess Postdoctoral Fellowship from Princeton University. Nicolas Cassar is supported by the "Laboratoire d'Excellence" LabexMER (ANR-10-LABX-19) and co-funded by a grant from the French government under the program "Investissements d'Avenir". Sarah Basart acknowledges the AXA Research Fund for the support of the long-term research line on Sand and Dust Storms at the Barcelona Supercomputing Center (BSC) and CAMS Global Validation (CAMS-84). Peter Strutton, Joan Llort, Morgane Perron and Andrew Bowie are supported by the Australian Research Council Discovery Projects scheme (DP190103504). Peter Strutton and Jakob Weis are supported by the Australian Research Council Centre of Excellence for Climate Extremes (CLEX: CE170100023). Joan Llort is supported by the European Union's Horizon 2020 research and

innovation programme under the Marie Skłodowska-Curie grant agreement No. 754433. Andrew Bowie is supported by the Australian Research Council Future Fellowship scheme (FT130100037). Richard Matear is supported by the CSIRO Decadal Climate Forecasting Project. We thank Michal Strzelec, Melanie East, Thomas Holmes, Matthew Corkill, Scott Meyerink and the Wellington Park Management Trust for help with installation and sampling the Tasmanian aerosol time-series station, and Ashley Townsend for iron aerosol analyses by ICPMS at the University of Tasmania. We would also like to thank Angela Benedetti and Samuel Remy for providing insights on the validation of aerosol reanalysis.

Author contributions

This study was conceived by N.C., J.L. and R.M. W.T. and N.C. wrote the manuscript with contribution from co-authors. J.L. and W.T. analyzed the spatial distribution and time-series of AOD, aerosol deposition and [Chl_a], and coordinated the interdisciplinary approach. J.W., C.S. and P. S. conducted the analysis of BGC-Argo float observations. S.B. and J.L. conducted the AOD decomposition reanalysis. Z.L. calculated MLD from Argo floats and estimated marine production with W.T. S.S. and T.J. provided and helped with interpretation of satellite observations of [Chl_a]. M. P., B.P. and A.B. collected the aerosol samples and analyzed the aerosol Fe content and solubility. E.S.R. analyzed levoglucosan in the aerosol samples. All authors contributed to the interpretation of the results.

Competing interests: The authors declare no competing interests.

Additional information

Supplementary information is available for this paper.

Correspondence and requests for materials should be addressed to R.M. and N. C.

Figure 1

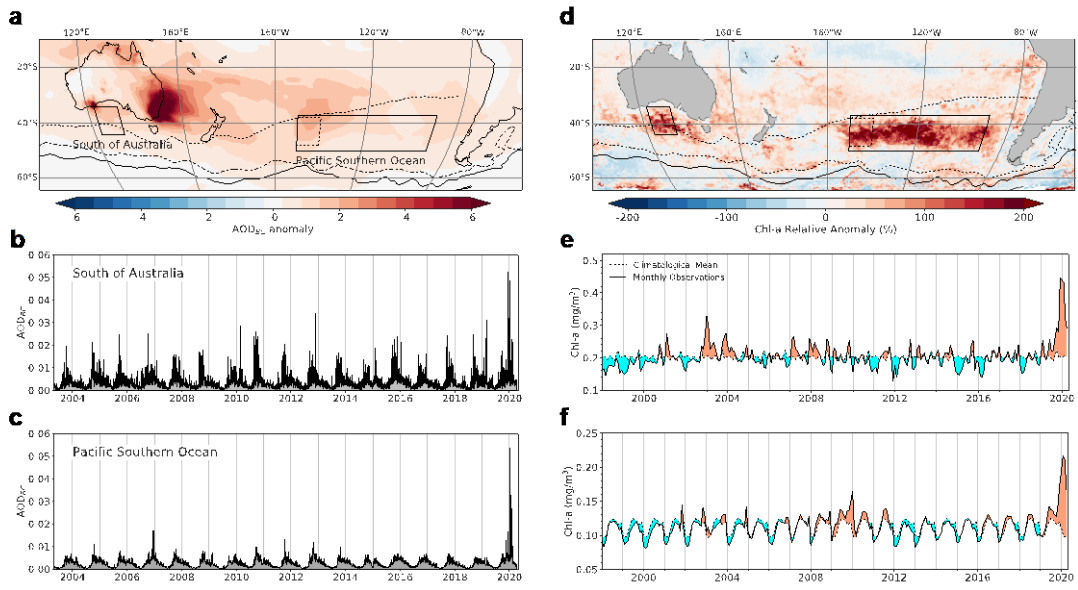


Figure 2

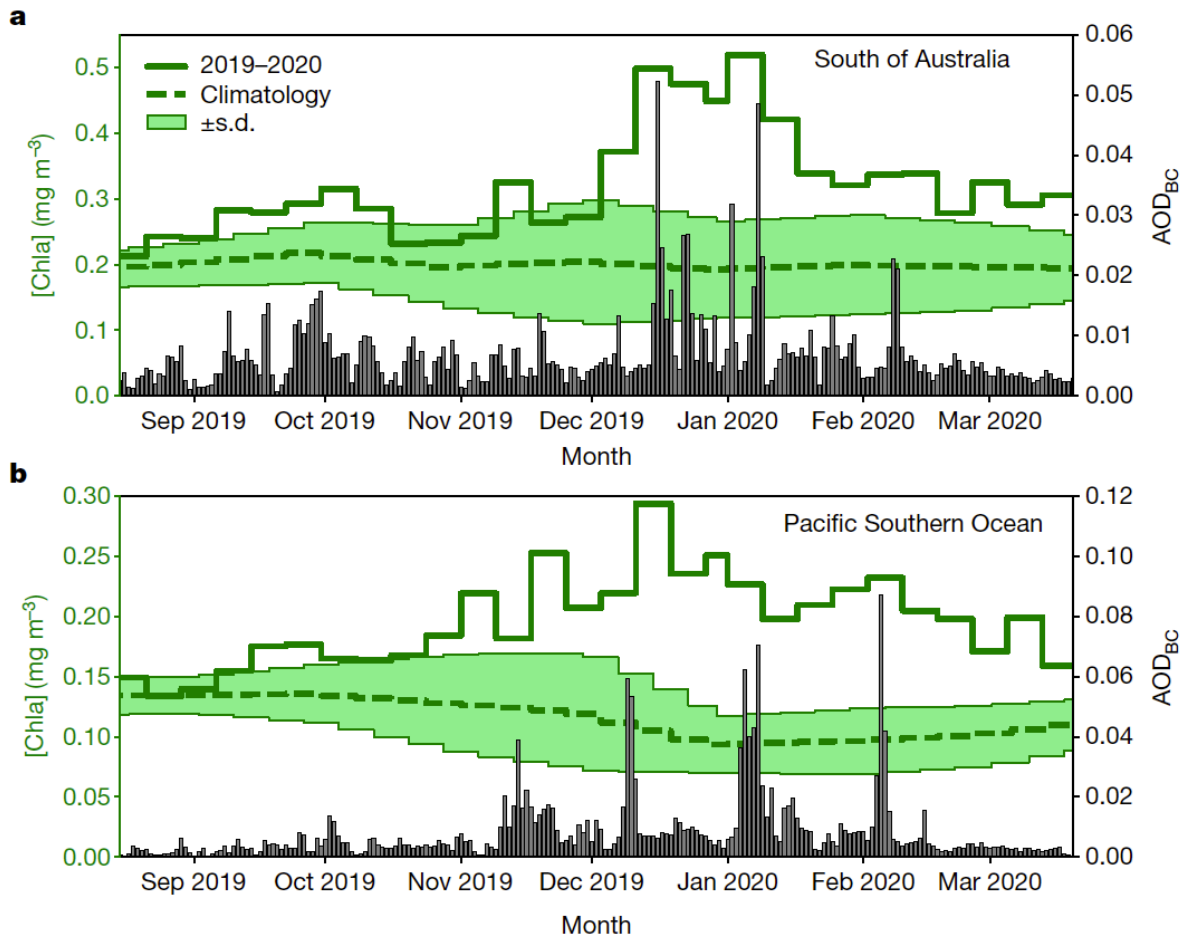


Figure 3

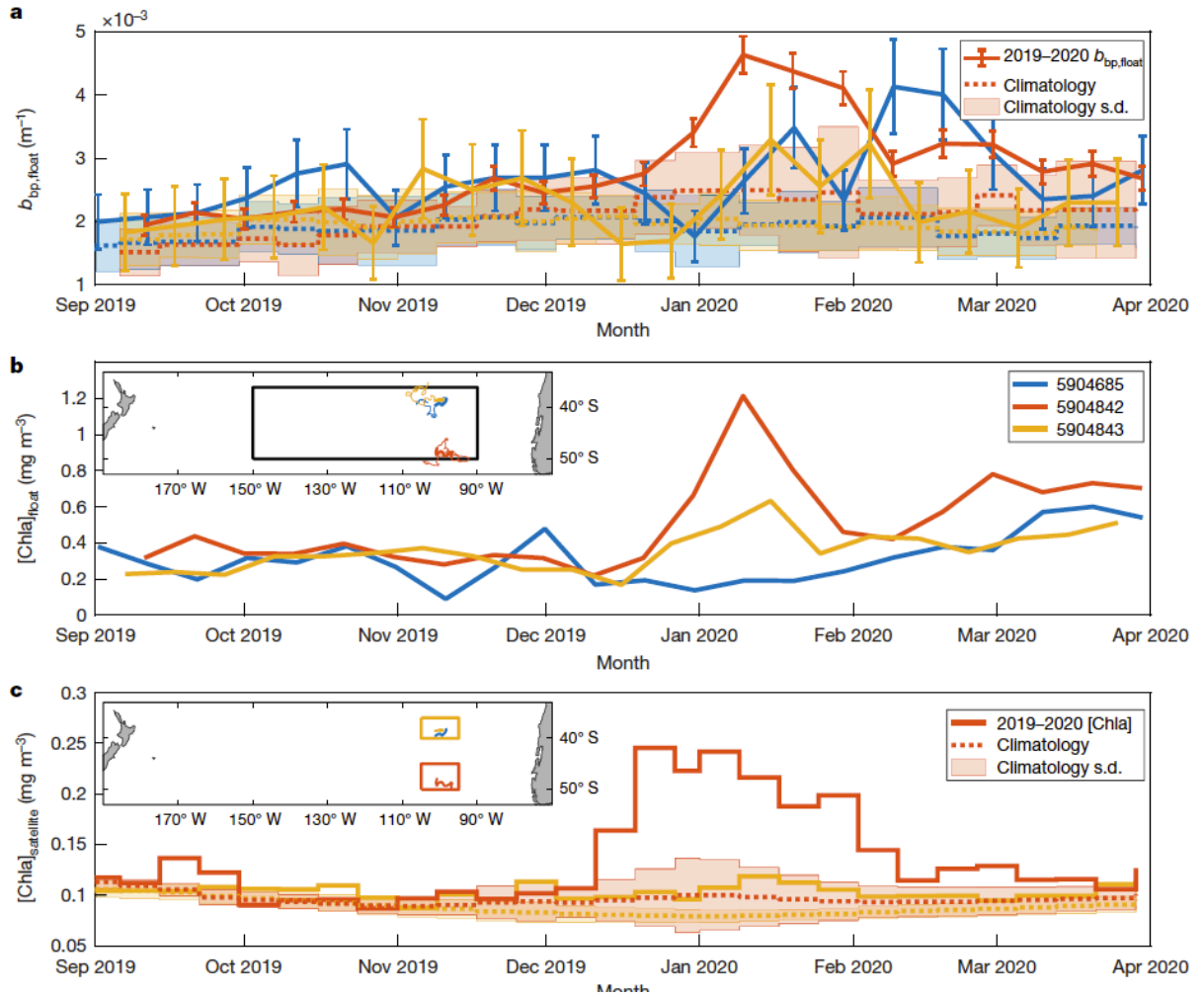


Figure 4

